Applied Physics B (2022) 128:63
https://doi.org/10.1007/s00340-022-07787-x

Applied Physics B
Lasers and Optics

Single-scan multiplane phase retrieval with a radiation of terahertz quantum cascade laser

Adrien Chopard[1,2] · Elizaveta Tsiplakova[3] · Nikolay Balbekin[3] · Olga Smolyanskaya[3] · Jean-Baptiste Perraud[4] · Jean-Paul Guillet[1] · Nikolay V. Petrov[3] · Patrick Mounaix[1]

Received: 5 January 2022 / Accepted: 17 February 2022

Abstract
Terahertz phase retrieval from a set of axially separated diffractive intensity distributions is a promising single-beam computational imaging technique that ensures the obtention of high spatial resolutions and phase wavefronts, but remains restricted by time-consuming data acquisition processes. In this work, we have adopted an approach, relying on the radiation of a quantum cascade laser and the implementation of an express single-scan measurement of intensity distributions through the continuous on-the-go displacement of a high-sensitivity antenna-coupled microbolometer sensor array. In addition to the simplicity of this practical implementation and the minimization of measurement times, such an approach overcomes the problem of preliminary optimal selections of transverse intensity distributions used in the iterative phase retrieval algorithm and guarantees the required data diversity for high-quality wavefront reconstruction.

1 Introduction

The increasing interest in the terahertz (THz) frequency range in recent decades has given rise to a new branch of techniques and algorithms for the non-contact evaluation of surface and subsurface features of various samples and materials. In this field, THz imaging [1–3] represents one of the most promising approaches, since it provides spatially resolved information about the investigated objects. THz phase imaging (THz PI) [4, 5], which includes pulse time-domain holography (PTDH) [6–22] as well as continuous wave (CW) holography [23–30], Hartmann wavefront sensing [31–35], shearorgaphy [36], ptychography [37–41], and other phase retrieval techniques [42–49], are currently under active development. A lot of technical solutions, experimental layouts, and reconstruction algorithms for THz PI have been proposed, and this field is reaching a certain level of maturity [5]. THz PTDH provides ultimate opportunities to track the dynamics of all the characteristics of a broadband THz field in spatial, temporal, spectral, and angular coordinates [50] during its interference [18, 19, 21] and propagation, both in free space [9, 12, 17, 22], through designed optical elements [51], obstacles [13, 20], and investigated objects [8, 10, 11, 16]. THz wavefront characterization with subsequent compensation through adaptive optics also serves as a compelling use case [52]. This technique requires femtosecond light sources and provides phase access via electro-optical sampling implemented using a reference near-infrared beam. The single-plane referenceless Hartmann method has been implemented with both CW [31–34] and pulsed [35] THz sources, but its scope is mainly related to wavefront sensing and analysis, while THz shearography, currently implemented with an IMPATT-diode, demonstrates similar capabilities, but promises to be also applicable to objects inspections [36]. In the light of those advances, lensless phase retrieval represents a compelling approach for nondestructive testing. More specifically, these techniques appear as a robust and sensitive tool for the assessment of optical properties and inhomogeneities in investigated samples, providing topographic insights through the retrieved wavefront phase

Adrien Chopard and Elizaveta Tsiplakova contributed equally to this work.

✉ Nikolay V. Petrov
n.petrov@niuitmo.ru

[1] IMS Laboratory, University of Bordeaux, UMR CNRS 5218, 351 Cours de la Libération Bâtiment A31, 33405 Talence, France

[2] Lytid SAS, 8 rue la Fontaine, 92120 Montrouge, France

[3] Institute of Photonics, ITMO University, Kronverkskiy 49, Saint-Petersburg 197101, Russia

[4] Optikan SAS, 64 rue Permentade, 33000 Bordeaux, France

Published online: 07 March 2022

profile, while rendering an accurate depiction of the object geometry. Equally important, the achievable spatial resolution of these wave approaches is often higher than that of standard raster-scanning focal plane imaging systems.

A multiple-plane phase retrieval is an efficient approach, which relies on the measurements of a set of axially separated transverse intensity distributions. Similar to the competing techniques, it also makes use of processing algorithms adapted from methodologies developed in the visible frequency range [42, 43]. The most popular algorithms are single-beam multiple intensity reconstruction (SBMIR) [53] and the transport of intensity equation [48]. This multiple-plane approach is characterized by the extreme simplicity of the object illumination setup and guarantees better convergence compared to single-plane phase retrieval algorithms, but the recording of the diffraction patterns often remains time-consuming.

Another problem that one has to face in multiple-plane phase retrieval in the THz frequency range is the existence of a narrow range of recording distances to the object for the optimal positioning of the sensor, from which it is possible to ensure the highest quality of the reconstructed images [43]. These optimal positions depend on the features of the diffraction process and can be generalized in terms of sets of dimensionless Fresnel numbers. It has been shown that registering intensity distributions with a too-small longitudinal pitch does not guarantee sufficient diversity in the data structure required for the convergence of the iterative algorithm [43]. Oppositely, the registration of transverse intensity distributions with excessively large longitudinal intervals does not lead to sufficiently high resolutions on the reconstructed images since the content of high spatial frequencies fades away for far-field diffraction. In general, the optimal longitudinal step when registering diffraction patterns separated along the optical axis depends on the diffraction zone, which is conveniently characterized by the distance between the object and the nearest intensity measurement plane.

In addition, it should be noted that the THz frequency range differs greatly from the visible wavelength range through the loss of the paraxial nature of the diffraction processes, which is usually caused by the small transverse dimension of a typical THz beam, with respect to the operating wavelength [20]. Thus, the choice of the optimal number and arrangement of measurements planes presents certain complexity and often have to be empirically assessed, and carried out through several series of experimental measurements or preliminary numerical simulations, hence remaining a time-consuming anticipation process.

And finally, success in solving practical problems of THz PI is guaranteed by the choice of a suitable combination of sources and detectors of radiation in this range of the electromagnetic spectrum. Early work on THz PI [4, 23–25, 28] used single-pixel detectors in the raster scan mode of operation due to the lack of matrix detectors. As array detectors became available, a larger variety of THz PI works initiated such implementations [54–58]. Nevertheless, the limited sensitivity of the THz radiation matrix detectors, along with the recurrent mismatches between the immutable pixel pitches and wavelengths of the detected THz radiation, do not allow the adaptation of existing solutions for an arbitrary combination of source and detector. To illustrate this point, a previous experiment demonstrated a multiple-plane phase retrieval setup in a reflection configuration based on a sequential raster scan using a single-pixel Shottky diode sensor, aiming to assess the diffraction pattern generated from up-converted Gunn diode at the wavelength of ~ 1 mm [53]. Other works, contrarily, made use of matrix detectors for the assessment of the set of intensity distributions in the diffraction field [48, 59], coupled to a high-power optically pumped far-infrared gas laser as the radiation source.

Thus, the given work aims to cover such technological shortcomings for multiple-plane phase retrieval, namely by overcoming (1) the currently limited demonstrations of source-detector combinations, the (2) time-consuming data acquisition, and the (3) necessity of preliminary optimizations of the experimental conditions. More specifically, we successfully demonstrate single beam multiple-plane iterative phase retrieval through the radiation of THz quantum cascade laser (QCL) and a real-time recording via a high-sensitivity antenna-coupled microbolometers camera. This experimental setup allows the express assessment of all the intensity distributions necessary for successful wavefront reconstruction in a unidirectional scan, with continuous acquisition implemented during a single longitudinal displacement of the array sensor. Thanks to the sensitive detection hardware, the implemented method is convenient and ensures an efficient way for data acquisition in on-the-go (OTG) mode. Hence, it eradicated the necessity of a preliminary choice concerning the optimal number and arrangement of measurements planes. It then guarantees the required data diversity for high-quality wavefront reconstruction and opens up the possibility for further automatic adjustment for the parameters of the iterative data processing.

2 Experimental implementation

In lensless computational diffractive THz PI, the bare bolometric array camera (‘C’ in Fig. 1), deprived of the imaging lens, can be employed for the simultaneous two-dimensional intensity distribution measurement in the transverse planes of the diffraction field. In a straightforward transmission configuration, such a recording unit should be complemented with the illumination source, required beam-shaping optics, sample holder (denoted as ‘O’ on Fig. 1), and the motorized translation stage (‘TS’) for the measurements of

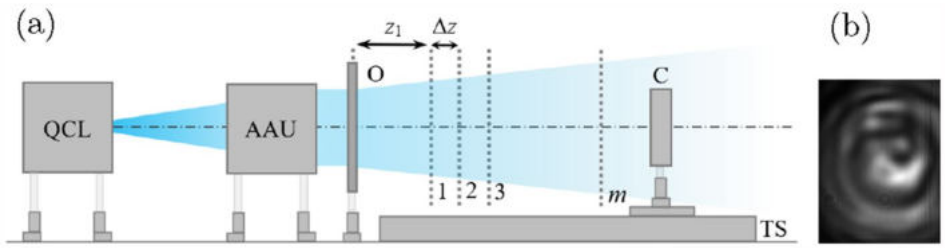

Fig. 1 Diagram of the experimental implementation for real-time phase retrieval measurement in transmission configuration (**a**) and the example of a formed far-field beam pattern, captured without object (**b**)

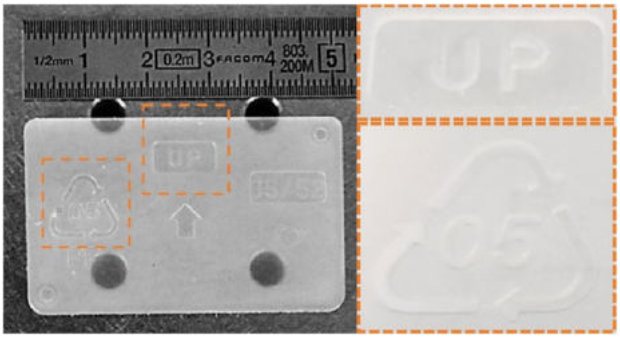

Fig. 2 Depiction of the PP Phase sample, investigated in this work, featuring two topographic RoI

the diffracted intensity profiles, $I_{z_k}(x, y)$, separated along the optical axis. In this work, Lytid's `TeraCascade 1000` QCL source, with an emission power of 1.3 mW at 2.5 THz, has been employed in combination with its integrated auto-alignment unit ('AAU' in Fig. 1) to provide a collimated illumination beam through 1" optics [2, 60].

Based on beam shaping optics and deflecting mirrors, Lytid's auto-alignment unit performs an automated source selection on the QCL multi-chip (there can be up to 6 chips in the Teracascade source). Then, from the diverging QCL's emission profile, it ensures the provision of a collimated beam, with a wavefront profile close to plane, to obtain a highly homogeneous illuminating wave phase, especially suitable for such applications. The example of the intensity distribution of the collimated beam captured without the object is shown in Fig. 1. Such a limited illumination diameter finds itself suitable when ranging up to 2.5 THz, with respect to lower frequencies implementations [53] that require larger inspection fields. Indeed, an obvious setup and sample rescale should be expected relative to the wavelength of operation.

In this transmission configuration of experimental layout, a polypropylene (PP) phase object (see Fig. 2) with thickness of 1.59 mm in unpatterned areas and a sample refractive index of $n_{\mathrm{PP}} = 1.5151$ at 2.5197 THz [41], has been investigated. Its specific topographic features display details of the order of the expected lateral resolution. Two regions of interest (RoI) of the sample were studied in this work: plastic identification code ('PIC') and 'UP' with grooved and extruded patterns, respectively, as shown in detail in the insets of Fig. 2.

A preliminary experiment has been performed using a first-generation INO IRXCAM camera (288×384 pixels matrix with 35 µm pitch), which displayed stability issues over the recording operations, hence limiting the measurement repeatability. Additionally, a drastic lack of sensitivity, coupled with the milliWatt illumination level, constrained the intensity recording to diffracted low spatial frequencies. The subsequent SBMIR wavefront extraction then only led to relevant reconstructions on restricted portions of the illumination field. The tenfold increase in sensitivity with the use of an *I2S* camera (240×320 pixels matrix with 50 µm pitch and detection rate 25 frames per second (FPS)) has then been employed for the suited recording of the intensity diffraction field data sets.

A prior stop-motion (SM) capture of the diffraction field, $I_{z_k}(x, y)$, was initially approached. The SM acquisition process is the conventional intensity distributions measurement mode, which consists of the sequential movement of the sensor for certain longitudinal steps Δz and the data recording in between these movements at the moments when the detector is stationary. It became widespread because it ensures the perfect mechanical stability of the sensor when recording, while potentially allowing for multi-frame averaging to improve the measurement SNR on each captured diffraction pattern (further, such an approach will be referred to as SM-A). As a rule of thumb, such capturing procedure takes to several minutes and the exact acquisition time depends on the desired number of frames used for averaging. In the case considered in this paper, we used a longitudinal pitch $\Delta z = 2$ mm, as featured in Fig. 3a, c and at each position, a set of roughly 35 images of the given diffraction patterns were captured for subsequent manual averaging. Due to the non-automated procedure, the time spent between every measurement for the sensor displacement varied. On average, the detector movement time interval was 2.184 ± 0.08 s. Therefore, the acquisition speed in the SM-A mode can be estimated as the number of pixels in the resulting averaged image of a certain measurement plane, with respect to the total movement and capturing time for the whole series of images being averaged. The result of the calculation is presented in Table 1. When not considering any additional averaging, the time spent on registering data in the SM

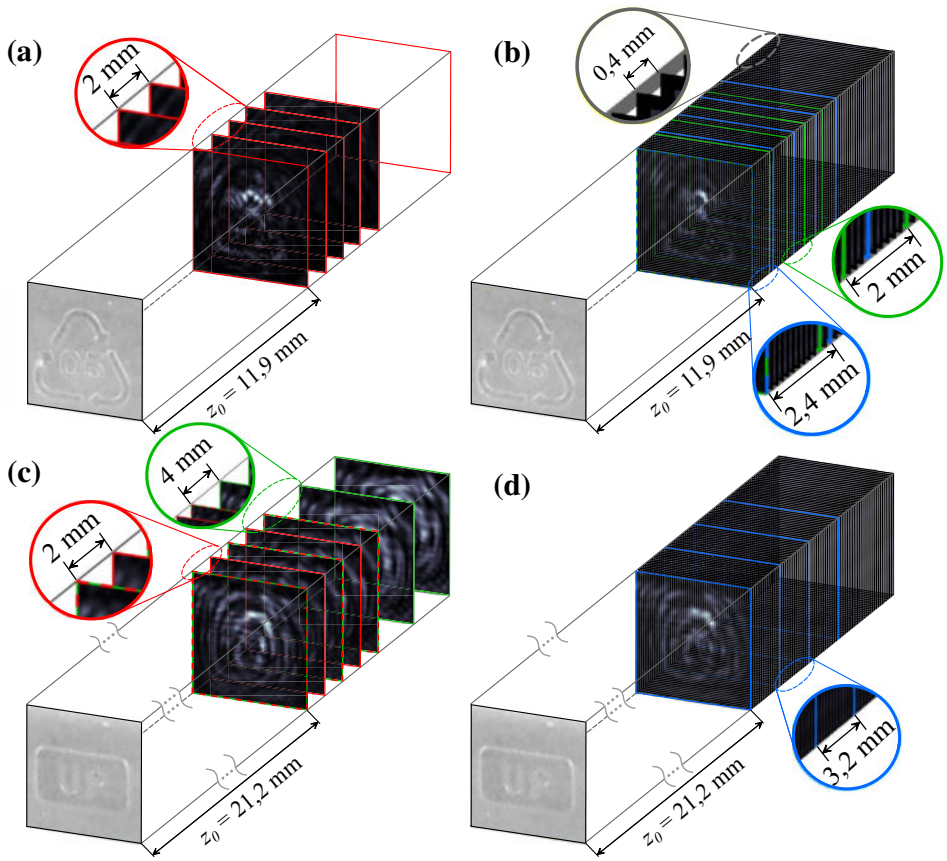

Fig. 3 Details for recording [SM-A (**a**, **c**) and OTG (**b**, **d**) modes] and utilizing (highlighted by RGB colors) data in an iterative algorithm for the object RoIs 'PIC' (**a**, **b**) and 'UP' (**c**, **d**), respectively

Table 1 Acquisition speed for various recording operation modes

Mode	RS	SM-A	SM-S	OTG
Source	GD FMC	QCL	QCL	QCL
Detector	SD	I2S	I2S	I2S
Speed, $\left(\frac{\text{pix}}{\text{s}}\right)$	12	2.10×10^4	3.45×10^4	1.92×10^6

mode theoretically can be neglected. We will refer to this option as SM-S, and the estimated acquisition speed for such approaches are presented in Table 1, notwithstanding we did not implement it in our experiments.

Featuring a continuous displacement of the sensor, the OTG data acquisition was also implemented. In this operating method, the movement of a motorized translation stage was initiated along with synchronization of the measurement process. Data acquisition with a continuous displacement of the sensor at the speed of 10 mm/s was defined as an optimal displacement speed in this implementation. It requires a recording time below 1 second for a longitudinal displacement of a few millimeters. Accounting for the recording rate of 25 FPS, a $\Delta z = 400$ µm longitudinal recording pitch is achieved for a raw recording data-set, as depicted in Fig. 3b, d. The acquisition speed for OTG mode then reaches 1.92×10^6 pix/s. Frame decimation in the diffraction profiles stack for the selection of an optimized input data-set for the SBMIR procedure can then be performed and refined as a post-processing operation.

The above-mentioned estimations of acquisition speed are then to be compared with the acquisition speed for the empirical single-pixel recording by raster scanning, implemented in previous work [53] (RS in Table 1).

3 Methods

From such diffraction fields recorded data-sets, displayed in Fig. 3, a square 240×240 pixel selection of the collected set, centered on the sample portion of the interest as well as the illumination beam, is cropped as to fit the subsequent algorithmic approach.

Namely, the straightforward sorted iterative SBMIR procedure features a strained propagation between measurement planes. The subsequent wavefront distributions are obtained via the employment of the free-space propagation kernel, $H(f_x,f_y)$, offered through the Fourier optics mechanism and employed as follows:

$$U(x,y,z) = \mathcal{F}^{-1}\left\{ H(f_x,f_y) \times \mathcal{F}\{U(x,y,0)\} \right\}, \quad (1)$$

where z is the arbitrary distance between the two subsequent planes, $U(x, y, 0)$ and $U(x, y, z)$ the complex amplitude of the wave front at the source plane and observation plane respectively. $\mathcal{F}$ and $\mathcal{F}^{-1}$ represents the direct and inverse Fourier transform operators respectively.

Regardless of any approximation, the general transfer function for free-space propagation over a distance z, $H(f_x,f_y)$, can be expressed as:

$$H(f_x,f_y) = \begin{cases} e^{i2\pi z\sqrt{\frac{1}{\lambda^2}-(f_x^2-f_y^2)}}, & \text{if } f_x^2+f_y^2 \leqslant \frac{1}{\lambda^2} \\ e^{-2\pi z\sqrt{\frac{1}{\lambda^2}-(f_x^2+f_y^2)}}, & \text{if } f_x^2+f_y^2 \geqslant \frac{1}{\lambda^2} \end{cases} \quad (2)$$

where $f_x = \frac{k_x}{2\pi}$ and $f_y = \frac{k_y}{2\pi}$ are the spatial frequency components in the Fourier space, along the $\vec{x}$ and $\vec{y}$ directions respectively, λ is the wavelength.

For each considered measurement plane, a constraint in amplitude is then applied as to fit the intensity diffracted field measurement such that $|U_{z_k}(x,y,z_k)| = \sqrt{I_{z_k}(x,y,z_k)}$ where U_{z_k} is the estimated complex field. This operation will then lead to the convergence of the wavefront phase profile along this iterative process.

Following this approach, a field focalization in the object plane can then be performed as to retrieve the object profile. Nevertheless, in such a configuration, a precise mechanical assessment of the first measurement plane distance, z_0, is impracticable due to the obstruction of the camera mechanical structure, as well as the unreachable sensor plane, lodged behind a protective window. Such a direct focused reconstruction on the object plane, following each SBMIR step, remains then inconceivable. The wavefront reconstruction has then to be performed at a raw estimated object plane position and further focused in a subsequent effort.

4 Results and discussion

The focused coherent field reconstructions, emerging from the SM-A recorded data-set and the proposed optimized OTG recording are displayed in Figs. 4 and 5 for two object's RoIs: PIC and UP respectively.

Figure 4 relates to the inspection of the PIC RoI through different SBMIR and data collection approaches. Namely, amplitude and phase images shown on Fig. 4a, d, correspondingly, were recovered from the first $m = 5$ intensity distributions of the dataset, obtained in SM-A mode, with the following parameters: $z_0 = 11.9$ mm, $\Delta z = 2$ mm. The use of only the first five input diffraction intensity distributions ensured the optimal quality of the reconstructed images while the inclusion of additional intensity distributions from more distant planes led to a worsening of the reconstruction quality, due to the lack of high spatial frequencies in that region. In addition, the single-frame captured for each of the measurement planes was extracted from the raw SM-A dataset (that is images before the averaging procedure) to simulate data recorded in SM-S mode. Negligible improvements have been witnessed when averaging over multiple still frames due to the adequacy of the emission power level with respect to the camera noise equivalent power.

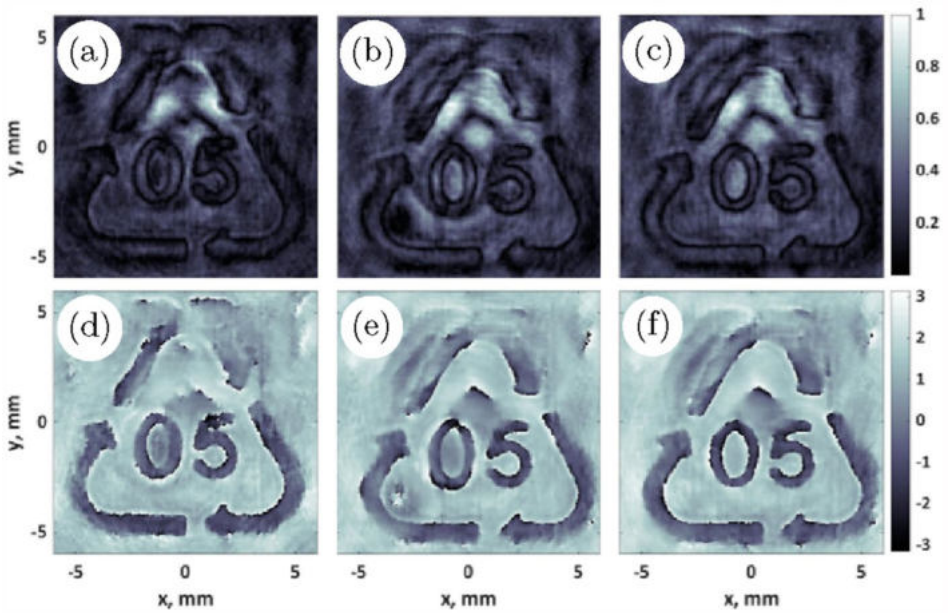

Fig. 4 Resulting numerical wavefront reconstruction, for amplitude (top rows) and phase (bottom rows) profiles, for 'PIC' RoI after 30 SBMIR iterations. The left column includes the data obtained using SM-A recording with $\Delta z = 2$ mm, while the middle and right columns, respectively, display wavefronts recovered using OTG recording with respective longitudinal pitches of $\Delta z = 2$ mm and at the optimal value of $\Delta z = 2.4$ mm

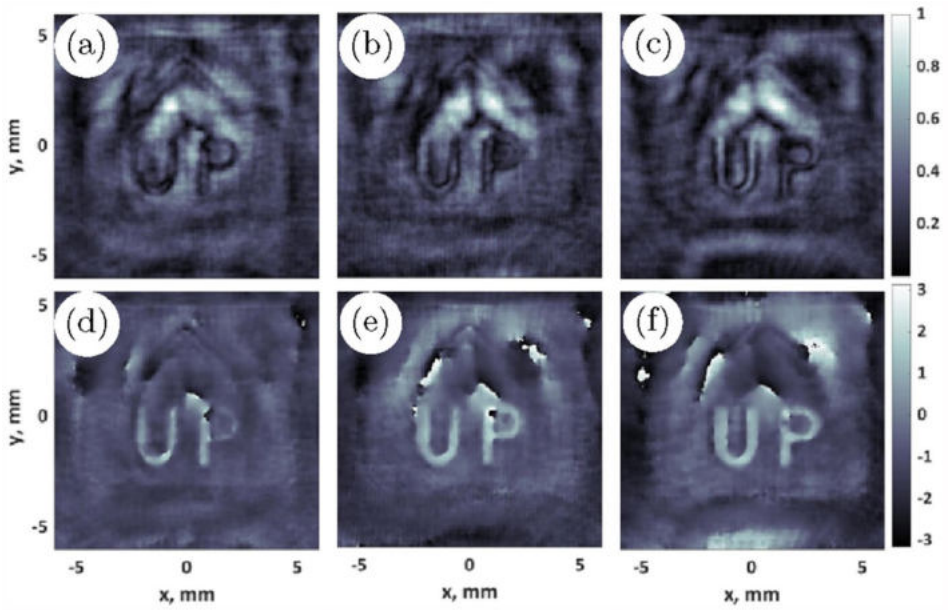

Fig. 5 Resulting numerical wavefront reconstruction, for amplitude (top rows) and phase (bottom rows) profiles, for 'UP' RoI after 50 iterations. The left and center columns include the data obtained using the SM-A recording method with $\Delta z = 2$ mm and $\Delta z = 4$ mm respectively while right column displays wavefronts recovered using the OTG recording method with an optimal longitudinal pitch of $\Delta z = 3.2$ mm

In the latest proposed OTG configuration, the 25 FPS detection rate of the camera allows for a continuous displacement of the planar array, while preventing any blurring effect during the sensor motion in the input data sets. Indeed, high requirements to the mechanical stability are critical in phase retrieval, implemented with the radiation of visible frequency range where the wavelength is less than the possible detector deviations caused by vibrations. In the THz frequency range, the radiation wavelength is much greater than the detector possible offsets range. That is why data recorded by a sensitive detector in OTG mode do not provide any deterioration of the reconstructed images. Herewith, at the previously mentioned frame rate, the achievable longitudinal pitch, $\Delta z = 400$ µm, remains beyond the required optimal value of recording spacing. It validated again, that, considering the smallest longitudinal pitch in the collected dataset does not necessarily lead to an optimal quality of the reconstructed images. This aspect has been extensively discussed in [43] as algorithmic optimizations have been assessed.

From the extensive OTG recordings, sub-datasets fitting the previous parameters, namely $\Delta z = 2$ mm, have been employed to reconstruct the wavefront, with amplitude and phase characteristics displayed in Fig. 4b, e. With respect to the slower SM-A recording, it stands out that the suitability of the proposed OTG acquisition mode, complemented with the collection of a decimated dataset selection, leads to the reconstruction of a slightly sharper coherent phase profile while a similar lateral resolution is obtained.

The versatility granted through the extensive data-set OTG capture is further highlighted in Fig. 4c, f. Indeed, further investigations demonstrated an optimal numerical longitudinal pitch of $\Delta z = 2.4$ mm, allowing to reach a representative wavefront recovery with once again $z_0 = 11.9$ mm and $m = 5$. Through the provision of such an exhaustive initial OTG input data, the optimal parameter set can then be empirically found in a post-processing task, preventing repetitive data registration to reach peak performances.

To endorse once gain the suitability of the proposed OTG approach, Fig. 5 confronts several processing configurations on the resulting reconstructions for the 'UP' RoI. More specifically, contrary to the previous configuration, a further investigation has been done, where the first intensity distribution was selected at distance $z_0 = 21.2$ mm. Such a more distant configuration has been motivated by the presence of practical cases where the location of the detector array close to the sample remains impracticable, for example, due to mechanical obstructions [61]. Similar restrictions take place in the case of the phase retrieval setups, operating in the reflection mode [53].

Since in the second experiment intensity, distributions were registered further from the object at the different diffraction subband, to reconstruct an image with the highest achievable quality, the optimal longitudinal pitch also should be reconsidered. Specifically, Fig. 5a, d and b, e display the reconstruction improvement when ranging from $\Delta z = 2$ mm to $\Delta z = 4$ mm through the initial SM-A capturing scheme, when considering $m = 5$ recording planes. However, due to the poor longitudinal resolution provided through this tedious and time-consuming acquisition process, no fine-tuning of this parameter of interest can be expected without additional experimental measurements. The OTG approach nevertheless provides a suitable alternative to such limitations. Indeed, an optimal wavefront, depicted in Fig. 5c, f,

has been reconstructed from a decimated input data-set featuring $\Delta z = 3.2$ mm.

Thus, in the light of the discussed results, it can be concluded, that the short recording longitudinal pitch, obtained through the high acquisition speed is especially suited as a prospective solution to be put to good use for the selection of an optimal SBMIR input data set, while allowing for fast full diffraction field assessment, under 1 second. Here, among this full recording, a numerical decimated set with $\Delta z = 2.4$ mm longitudinal pitch has been found to be optimal for the 'PIC' sample, hence considering 1 out of 5 400 µm discreet diffraction profiles. The further assessment of the diffraction field led to an optimal longitudinal pitch of $\Delta z = 3.2$ mm for the 'UP' RoI.

Nevertheless, independently of the recording approach, those results display wavefront inhomogeneities in their phase and amplitude profiles. Those features can be devolved to the probe beam wavefront inhomogeneities, even though the careful beam shaping of the auto-alignment unit ensures the generation of a collimated plane wavefront from the diverging beam profile of the emission QCL. Indeed, the beam profile differs from Gaussian one, as shown in Fig. 1. These inhomogeneities can include wavefront singularities, negatively affecting the construction of a surface topography map. Nevertheless, knowing the spatial coordinates of the area with the most pronounced parasitic wavefront curvature, it is sometimes possible to implement a numerical correction procedure (Fig. 6a). However, it is not always convenient. Therefore, at some phase maps the impact of the parasitic wavefront curvature may remain uncorrected, leading to errors in a surface profile (Fig. 6b). Topographic variations between the unpatterned and grooved areas for the 'PIC' RoI and between the background and the extruded letters 'UP' are about 200 µm and 100 µm, respectively.

Beyond the addressed coherent imaging perspectives, the employment of such real-time recording techniques to provide coherent wavefront distribution can as well be put to good use for source characterizations and far-field wavefront sensing. It would indeed overcome the limited resolution of the sub-samples Hartman method [31–34], tied to the hole-punched mask and sensor pitch. In the case of QCL radiation, the wavefront of which still contains singular points after collimation, multiple-plane phase retrieval the can be easily implemented. However, in the case of the smooth, non-diffracting wavefront, the basic SBMIR algorithm became inefficient for wavefront sensing. To deal with this problem a small controlled disturbance must be introduced into the examined wavefront, which can be removed afterward from retrieved phase distribution, as was demonstrated in [53].

5 Conclusion

The tedious multi-plane data collection process, required for the SBMIR algorithmic approach remains a major drawback of such iterative phase retrieval procedures. Through a simplified transmission configuration, featuring a high-power QCL adequately coupled to a highly sensitive camera sensor, a real-time recording with the continuous displacement of the sensor allows OTG acquisition of the full diffraction field, eligible for high-quality reconstruction. Such a fast recording process, ensures the collection of an exhaustive dataset that provides substantial flexibility in the post-processing extraction steps of the wavefront. Namely, the importance of the selection of the numerical longitudinal pitch, Δ_z, on the reconstruction quality has already been highlighted and the OTG recording allows this parameter to undergo an optimization in post-processing operations, preventing time-consuming iterative experimental tasks.

Beyond the scope of this work, a few limitations remain discernible on the wavefront reconstructions. Namely edge effects, induced by the limited sensor dimensions are impacting the wavefront uniformity. Through algorithmic extrapolation procedures [16, 62], or experimentally, with the mapping of a wider imaging field through the lateral displacement of the camera [27, 63] combined with the longitudinal multi-plane OTG recording, the enhanced retrieval of complex wavefront profiles would be expected.

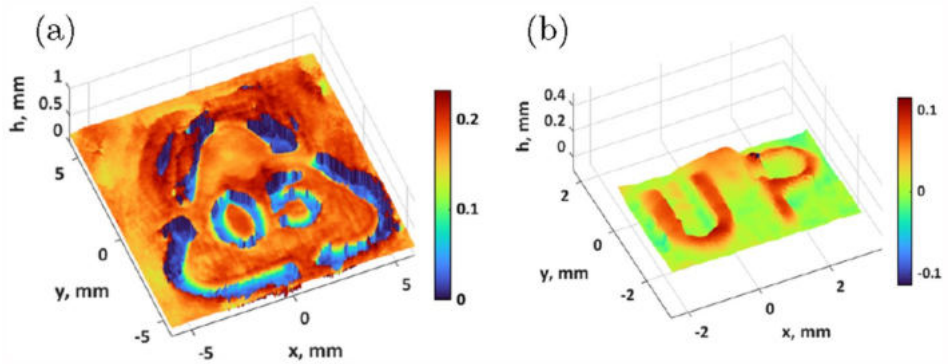

Fig. 6 Reconstructed surface map phase for the RoI 'PIC' (**a**) and 'UP' (**b**)

Acknowledgements This work was supported by the Russian Foundation for Basic Research and Centre National de la Recherche Scientifique under grant No. 21-52-15035/21.

References

1. G. Valušis, A. Lisauskas, H. Yuan, W. Knap, H.G. Roskos, Roadmap of terahertz imaging 2021. Sensors **21**(12), 4092 (2021)
2. J.-B. Perraud, A. Chopard, J.-P. Guillet, P. Gellie, A. Vuillot, P. Mounaix, A versatile illumination system for real-time terahertz imaging. Sensors **20**(14), 3993 (2020)
3. N.V. Chernomyrdin, M. Skorobogatiy, A.A. Gavdush, G.R. Musina, G.M. Katyba, G.A. Komandin, A.M. Khorokhorov, I.E. Spektor, V.V. Tuchin, K.I. Zaytsev, Quantitative super-resolution solid immersion microscopy via refractive index profile reconstruction. Optica **8**(11), 1471 (2021)
4. N.V. Petrov, A.A. Gorodetsky, V.G. Bespalov, Holography and phase retrieval in terahertz imaging. Proc. SPIE **8846**, 88460S (2013)
5. M. Wan, J.J. Healy, J.T. Sheridan, Terahertz phase imaging and biomedical applications. Opt. Laser Technol. **122**, 105859 (2020)
6. V.G. Bespalov, A.A. Gorodetskiĭ, Modeling of referenceless holographic recording and reconstruction of images by means of pulsed terahertz radiation. J. Opt. Technol. **74**(11), 745 (2007)
7. Y. Zhang, W. Zhou, X. Wang, Y. Cui, W. Sun, Terahertz digital holography. Strain **44**(5), 380–385 (2008)
8. N.S. Balbekin, E.V. Novoselov, P.V. Pavlov, V.G. Bespalov, N.V. Petrov, Nondestructive monitoring of aircraft composites using terahertz radiation. Proc. SPIE **9448**, 94482D (2015)
9. N. Balbekin, M. Kulya, P. Rogov, N. Petrov, The modeling peculiarities of diffractive propagation of the broadband terahertz two-dimensional field. Phys. Procedia **73**, 49–53 (2015)
10. N.V. Petrov, M.S. Kulya, A.N. Tsypkin, V.G. Bespalov, A. Gorodetsky, Application of terahertz pulse time-domain holography for phase imaging. IEEE Trans. Terahertz Sci. Technol. **6**(3), 464–472 (2016)
11. M.S. Kulya, N.S. Balbekin, I.V. Gredyuhina, M.V. Uspenskaya, A.P. Nechiporenko, N.V. Petrov, Computational terahertz imaging with dispersive objects. J. Mod. Opt. **64**(13), 1283–1288 (2017)
12. M.S. Kulya, V.A. Semenova, V.G. Bespalov, N.V. Petrov, On terahertz pulsed broadband Gauss–Bessel beam free-space propagation. Sci. Rep. **8**(1), 1390 (2018)
13. M. Kulya, V. Semenova, A. Gorodetsky, V.G. Bespalov, N.V. Petrov, Spatio-temporal and spatiospectral metrology of terahertz broadband uniformly topologically charged vortex beams. Appl. Opt. **58**(5), A90 (2019)
14. M. Kulya, N.V. Petrov, A. Tsypkin, K. Egiazarian, V. Katkovnik, Hyperspectral data denoising for terahertz pulse time-domain holography. Opt. Express **27**(13), 18456 (2019)
15. M. Kulya, N.V. Petrov, V. Katkovnik, K. Egiazarian, Terahertz pulse time-domain holography with balance detection: complex-domain sparse imaging. Appl. Opt. **58**(34), G61–G70 (2019)
16. N.S. Balbekin, M.S. Kulya, A.V. Belashov, A. Gorodetsky, N.V. Petrov, Increasing the resolution of the reconstructed image in terahertz pulse time-domain holography. Sci. Rep. **9**(1), 180 (2019)
17. M.S. Kulya, N.S. Balbekin, A.A. Gorodetsky, S.A. Kozlov, N.V. Petrov, Vectorial terahertz pulse time-domain holography for broadband optical wavefront sensing. Proc. SPIE **11279**, 112790D (2020)
18. M.S. Kulya, B. Sokolenko, A. Gorodetsky, N.V. Petrov, Propagation dynamics of ultrabroadband terahertz beams with orbital angular momentum for wireless data transfer. Proc. SPIE **11307**, 113070J (2020)
19. N.V. Petrov, M.S. Kulya, A.A. Gorodetsky, B. Sokolenko, On the features of the interference of a set of broadband uniformly topologically charged beams. Proc. SPIE **11499**, 114990I (2020)
20. X. Liu, M.S. Kulya, N.V. Petrov, Y.V. Grachev, M. Song, A.N. Tcypkin, S.A. Kozlov, X.-C. Zhang, Spectral Fresnel filter for pulsed broadband terahertz radiation. AIP Adv. **10**(12), 125104 (2020)
21. E.G. Tsiplakova, M.S. Kulya, B.V. Sokolenko, A.A. Gorodetsky, N.V. Petrov, Investigation of spectral encoding with terahertz broadband uniformly topologically charged beams. in *2021 46th International Conference on Infrared, Millimeter and Terahertz Waves (IRMMW-THz)*, pp. 1–2, IEEE, (2021)
22. Y.V. Grachev, V.A. Kokliushkin, N.V. Petrov, Open-source 3D-printed terahertz pulse time-domain holographic detection module. Applied Optics **61**(5), B307 (2022)
23. R.J. Mahon, J.A. Murphy, W. Lanigan, Digital holography at millimetre wavelengths. Optics Communications **260**(2), 469–473 (2006)
24. A. Tamminen, J. Ala-Laurinaho, A.V. Räisänen, Indirect holographic imaging: evaluation of image quality at 310 GHz. Proceedings of SPIE **7670**, 76700A (2010)
25. M.S. Heimbeck, M.K. Kim, D.A. Gregory, H.O. Everitt, Terahertz digital holography using angular spectrum and dual wavelength reconstruction methods. Optics Express **19**(10), 9192–9200 (2011)
26. K. Xue, Q. Li, Y.-D. Li, Q. Wang, Continuous-wave terahertz in-line digital holography. Optics Letters **37**(15), 3228 (2012)
27. Z. Li, R. Zou, W. Kong, X. Wang, Q. Deng, Q. Yan, Y. Qin, W. Wu, X. Zhou, Terahertz synthetic aperture in-line holography with intensity correction and sparsity autofocusing reconstruction. Photonics Research **7**(12), 1391 (2019)
28. M.S. Heimbeck, W.-R. Ng, D.R. Golish, M.E. Gehm, H.O. Everitt, Terahertz Digital Holographic Imaging of Voids Within Visibly Opaque Dielectrics. IEEE Transactions on Terahertz Science and Technology **5**(1), 110–116 (2015)
29. Y. Zhang, J. Zhao, D. Wang, Y. Wang, L. Rong, Lensless Fourier-transform terahertz digital holography for real-time full-field phase imaging. Photonics Research **10**(2), 323 (2022)
30. D. Wang, D. Ma, K. Li, Y. Zhang, J. Zhao, Y. Wang, L. Rong, Dynamic full-field refractive index distribution measurements using total internal reflection terahertz digital holography. Photonics Research **10**(2), 289 (2022)
31. M. Cui, J.N. Hovenier, Y. Ren, A. Polo, J.R. Gao, Terahertz wavefronts measured using the Hartmann sensor principle. Optics Express **20**(13), 14380 (2012)
32. H. Richter, M. Greiner-Bär, N. Deßmann, J. Pfund, M. Wienold, L. Schrottke, R. Hey, H.T. Grahn, H.-W. Hübers, Terahertz wavefront measurement with a Hartmann sensor. Applied Physics Letters **101**(3), 031103 (2012)
33. M. Cui, J.N. Hovenier, Y. Ren, N. Vercruyssen, J.R. Gao, T.Y. Kao, Q. Hu, J.L. Reno, Beam and phase distributions of a terahertz quantum cascade wire laser. Applied Physics Letters **102**(11), 111113 (2013)
34. H. Richter, N. Rothbart, H.W. Hübers, Characterizing the beam properties of terahertz quantum-cascade lasers. Journal of Infrared, Millimeter, and Terahertz Waves **35**(8), 686–698 (2014)
35. E. Abraham, H. Cahyadi, M. Brossard, J. Degert, E. Freysz, T. Yasui, Development of a wavefront sensor for terahertz pulses. Optics Express **24**(5), 5203 (2016)
36. M.Agour, C.Fallorf, F.Taleb, E.Castro-Camus, M.Koch, R.B. Bergmann, "Terahertz referenceless wavefront sensing by means of computational shear-interferometry," *Optics Express* **Vol. TBD**, p. (Accepted), (2022)
37. L. Valzania, T. Feurer, P. Zolliker, E. Hack, Terahertz ptychography. Optics Letters **43**(3), 543–546 (2018)

38. L.Valzania, E.Hack, P.Zolliker, R.Brönnimann, T.Feurer, "Resolution limits of terahertz ptychography," in *Unconventional Optical Imaging*, **10677**, p. 1067720, International Society for Optics and Photonics, (2018)
39. L. Rong, C. Tang, Y. Zhao, F. Tan, Y. Wang, J. Zhao, D. Wang, M. Georges, Continuous-wave terahertz reflective ptychography by oblique illumination. Optics Letters **45**(16), 4412–4415 (2020)
40. D. Wang, B. Li, L. Rong, F. Tan, J.J. Healy, J. Zhao, Y. Wang, Multi-layered full-field phase imaging using continuous-wave terahertz ptychography. Optics Letters **45**(6), 1391–1394 (2020)
41. L. Rong, F. Tan, D. Wang, Y. Zhang, K. Li, J. Zhao, Y. Wang, High-resolution terahertz ptychography using divergent illumination and extrapolation algorithm. Optics and Lasers in Engineering **147**, 106729 (2021)
42. N.V. Petrov, V.G. Bespalov, M.V. Volkov, Phase retrieval of thz radiation using set of 2d spatial intensity measurements with different wavelengths. Proceedings of SPIE **8281**, 82810J (2012)
43. N.V. Petrov, A.N. Galiaskarov, T.Y. Nikolaeva, V.G. Bespalov, The features of optimization of a phase retrieval technique in THz frequency range. Proceedings of SPIE **8413**, 84131T (2012)
44. G. Junkin, Planar near-field phase retrieval using GPUs for accurate THz far-field prediction. IEEE Transactions on Antennas and Propagation **61**(4), 1763–1776 (2012)
45. X. Gao, C. Li, G.-Y. Fang, The Realization of Terahertz Image Reconstruction with High Resolution Based on the Amplitude of the Echoed Wave by using the Phase Retrieval Algorithm. Chinese Optics Letters **30**(6), 068401 (2013)
46. J. Hu, Q. Li, S. Cui, Research on object-plane constraints and hologram expansion in phase retrieval algorithms for continuous-wave terahertz inline digital holography reconstruction. Applied Optics **53**(30), 7112 (2014)
47. Y. Ren, G. Xie, Y. Zhang, D. Liu, K. Zhou, W. Miao, W. Zhang, S. Shi, Development of terahertz two-dimensional phase gratings for multiple beam generation based on a high-accuracy phase retrieval algorithm. Optics Express **29**(12), 17951–17961 (2021)
48. L. Rong, S. Wang, D. Wang, F. Tan, Y. Zhang, J. Zhao, Y. Wang, Transport of intensity equation-based terahertz lensless full-field phase imaging. Optics Letters **46**(23), 5846–5849 (2021)
49. X. Jin, J. Zhao, D. Wang, L. Rong, Y. Wang, J.J. Healy, S. Lin, Iterative denoising phase retrieval method for twin-image elimination in continuous-wave terahertz in-line digital holography. Optics and Lasers in Engineering **152**, 106986 (2022)
50. J.T. Sheridan, R.K. Kostuk, A.F. Gil, Y. Wang, W. Lu, H. Zhong, Y. Tomita, C. Neipp, J. Francés, S. Gallego, I. Pascual, V. Marinova, S. Lin, K.-Y. Hsu, F. Bruder, S. Hansen, C. Manecke, R. Meisenheimer, C. Rewitz, T. Rölle, S. Odinokov, O. Matoba, M. Kumar, X. Quan, Y. Awatsuji, P.W. Wachulak, A.V. Gorelaya, A.A. Sevryugin, E.V. Shalymov, V. Yu Venediktov, R. Chmelik, M.A. Ferrara, G. Coppola, A. Márquez, A. Beléndez, W. Yang, R. Yuste, A. Bianco, A. Zanutta, C. Falldorf, J.J. Healy, X. Fan, B.M. Hennelly, I. Zhurminsky, M. Schnieper, R. Ferrini, S. Fricke, G. Situ, H. Wang, A.S. Abdurashitov, V.V. Tuchin, N.V. Petrov, T. Nomura, D.R. Morim, K. Saravanamuttu, Roadmap on holography. Journal of Optics **22**(12), 123002 (2020)
51. N.V. Petrov, B.Sokolenko, M.S. Kulya, A. Gorodetsky, A.V. Chernykh, "Broadband THz vector and vortex beams: II. Holographic tools for numeric assessment," *Light: Advanced Manufacturing* **Vol. TBD**(Submitted), (2022)
52. M. Brossard, J.-F. Sauvage, M. Perrin, E. Abraham, Terahertz adaptive optics with a deformable mirror. Optics Letters **43**(7), 1594–1597 (2018)
53. N.V. Petrov, J.-B. Perraud, A. Chopard, J.-P. Guillet, O.A. Smolyanskaya, P. Mounaix, Terahertz phase retrieval imaging in reflection. Optics Letters **45**(15), 4168–4171 (2020)
54. Q. Li, S.-H. Ding, Y.-D. Li, K. Xue, Q. Wang, Research on Reconstruction Algorithms in 2.52 THz Off-axis Digital Holography. Journal of Infrared, Millimeter, and Terahertz Waves **33**(10), 1039–1051 (2012)
55. E. Hack, L. Valzania, G. Gäumann, M. Shalaby, C.P. Hauri, P. Zolliker, Comparison of thermal detector arrays for off-axis THz holography and real-time THz imaging. Sensors **16**(2), 221 (2016)
56. S.-H. Ding, Q. Li, Y.-D. Li, Q. Wang, Continuous-wave terahertz digital holography by use of a pyroelectric array camera. Optics Letters **36**(11), 1993–1995 (2011)
57. P. Zolliker, E. Hack, THz holography in reflection using a high resolution microbolometer array. Optics Express **23**(9), 10957–10967 (2015)
58. M. Locatelli, M. Ravaro, S. Bartalini, L. Consolino, M.S. Vitiello, R. Cicchi, F. Pavone, P. De Natale, Real-time terahertz digital holography with a quantum cascade laser. Scientific Reports **5**(1), 1–7 (2015)
59. L. Valzania, P. Zolliker, E. Hack, Coherent reconstruction of a textile and a hidden object with terahertz radiation. Optica **6**(4), 518–523 (2019)
60. https://lytid.com/optics/optical-modules/auto-alignment module. Last accessed Feb.01,2022
61. G. Pedrini, I. Alekseenko, G. Jagannathan, M. Kempenaars, G. Vayakis, W. Osten, Feasibility study of digital holography for erosion measurements under extreme environmental conditions inside the International Thermonuclear Experimental Reactor tokamak [invited]. Applied Optics **58**(5), A147 (2019)
62. Z. Li, Q. Yan, Y. Qin, W. Kong, M. Zou, X. Zhou, Z. You, P. Cheng, Resolution enhancement in terahertz digital in-line holography by sparsity-based extrapolation. Journal of Infrared, Millimeter, and Terahertz Waves **42**(5), 479–492 (2021)
63. H. Huang, D. Wang, W. Li, L. Rong, Z.D. Taylor, Q. Deng, B. Li, Y. Wang, W. Wu, S. Panezai, Continuous-wave terahertz multiplane in-line digital holography. Optics and Lasers in Engineering **94**(100), 76–81 (2017)